Preprint
UCRL-JC-139805

The Validity of a Paraxial Approximation in the Simulation of Laser-Plasma Interactions

E. McKay Hyde

This article was submitted to
Student Symposium 2000, Albuquerque, NM, August 10, 2000

July 26, 2000

U.S. Department of Energy

Lawrence
Livermore
National
Laboratory

The Validity of a Paraxial Approximation in the Simulation of Laser-Plasma Interactions

E. McKay Hyde[1]

Applied Mathematics
California Institute of Technology
Pasadena, CA 91125

Work supervised by

Milo R. Dorr and F. Xabier Garaizar

Center for Applied Scientific Computing
Lawrence Livermore National Laboratory
Livermore, CA 94550

July 26, 2000

[1]This work was performed under the auspices of the U.S. Department of Energy by University of California Lawrence Livermore National Laboratory under contract No. W-7405-Eng-48.

This page was left blank intentionally

1 Introduction

The design of high-power lasers such as those used for inertial confinement fusion demands accurate modeling of the interaction between lasers and plasmas. In inertial confinement fusion, initial laser pulses ablate material from the hohlraum, which contains the target, creating a plasma. Plasma density variations due to plasma motion, ablating material and the ponderomotive force exerted by the laser on the plasma disrupt smooth laser propagation, undesirably focusing and scattering the light. Accurate and efficient computational simulations aid immensely in developing an understanding of these effects.

In this paper, we compare the accuracy of two methods for calculating the propagation of laser light through plasmas. A full laser-plasma simulation typically consists of a fluid model for the plasma motion and a laser propagation model. These two pieces interact with each other as follows. First, given the plasma density, one propagates the laser with a refractive index determined by this density. Then, given the laser intensities, the calculation of one time step of the plasma motion provides a new density for the laser propagation. Because this procedure repeats over many time steps, each piece must be performed accurately and efficiently.

In general, calculation of the light intensities necessitates the solution of the Helmholtz equation with a variable index of refraction. The Helmholtz equation becomes extremely difficult and time-consuming to solve as the problem size increases. The size of laser-plasma problems of present interest far exceeds current capabilities.

To avoid solving the full Helmholtz equation one may use a paraxial approximation. Generally speaking the paraxial approximation applies when one expects negligible backscattering of the light and only mild scattering transverse to the direction of light propagation. This approximation results in a differential equation that is first-order in the propagation direction that can be integrated accurately and efficiently even for large computational domains.

This paper explores the domain of validity of a paraxial approximation in laser-plasma simulations. High-intensity lasers may create high-density plasmas and induce extremely large and abrupt plasma density variations. Such variations in high-density plasmas can reflect or scatter a significant fraction of the incident light. However, as stated, the paraxial approximation assumes negligible backscatter. Furthermore, interference of incident and scattered waves may produce regions of high-intensity light that the paraxial approximation fails to predict accurately. Certainly, the paraxial approximation serves as an excellent approximation in many problems. We hope to provide insight into when it accurately models the problem and when it does not.

To explore the validity of the approximation we compare the Helmholtz equation solution to the paraxial wave equation solution for a variety of fixed plasma densities on a reduced computational domain. As stated above, a time-dependent comparison on a large computational domain is currently infeasible. We first introduce the pertinent physical equations. We then derive the paraxial approximation, highlighting the approximating assumptions. A brief explanation of the numerical methods follows. Finally, we present a graphical comparison of the solutions for several examples.

2 Electromagnetic Waves in Plasmas

We now discuss the applicable equations for the light propagation and the ponderomotive force. Furthermore, we examine the reflection of light from sharp interfaces. This lends insight into when we should expect significant reflection and the effect this has on laser intensity.

2.1 Relevant Equations

We sketch a derivation of the relevant equations following [7]. (See also [8, p. 7–31], [1, p. 2245] and [9, p. 141–144].) The microscopic formulation of Maxwell's equations reads

$$\nabla \cdot \mathbf{E} = \frac{\rho}{\epsilon_0}, \tag{1}$$

$$\nabla \cdot \mathbf{B} = 0, \tag{2}$$

$$\nabla \times \mathbf{E} = -\frac{\partial \mathbf{B}}{\partial t}, \tag{3}$$

$$\nabla \times \mathbf{B} = \mu_0 \mathbf{J} + \frac{1}{c^2}\frac{\partial \mathbf{E}}{\partial t}. \tag{4}$$

(Note that $\mu_0 \epsilon_0 c^2 = 1$.) Taking the curl of (3) and substituting (4) into the result gives

$$(\Delta \mathbf{E} - \frac{1}{c^2}\frac{\partial^2 \mathbf{E}}{\partial t^2}) - \nabla(\nabla \cdot \mathbf{E}) - \mu_0 \frac{\partial \mathbf{J}}{\partial t} = 0. \tag{5}$$

We neglect ion oscillations due to the electromagnetic wave because they are much more massive than the electrons. Hence, only the electron motion due to the wave contributes to the current, $\mathbf{J}$. Assume that the electrons and ions have velocities $\mathbf{v}$ and $\mathbf{v_0}$, respectively. Then, let

$$\mathbf{v}' = \mathbf{v} - \mathbf{v_0}. \tag{6}$$

This implies that

$$\mathbf{J} = -ne\mathbf{v}', \tag{7}$$

where e and n give the electron charge and number density, respectively. Finally, we assume that the electrons undergo only small perturbations to some background density, pressure and temperature. Then, the following approximates the electron equation of motion.

$$m\frac{\partial \mathbf{v}}{\partial t} = m\frac{\partial \mathbf{v}'}{\partial t} = -e\mathbf{E}, \tag{8}$$

where m is the electron mass.

Remark. We have followed common practice in neglecting the convective term, the Lorentz force, ion-electron collisions and the pressure gradient term in the electron equation of motion. However, some question remains as to whether we may neglect these terms in some situations that we consider in this paper, namely, large, sharp variations in the relatively high plasma densities.

Assuming a time-harmonic solution, $\mathbf{E}(\mathbf{x}, t) = \mathbf{E}'(\mathbf{x})e^{-i\omega t}$, and combining equations (5), (7) and (8), we arrive at

$$\Delta \mathbf{E} + k^2\left(1 - \frac{w_p^2(\mathbf{x})}{w^2}\right)\mathbf{E} - \nabla(\nabla \cdot \mathbf{E}) = 0, \tag{9}$$

where $w_p^2 = \frac{e^2 n(\mathbf{x})}{\epsilon_0 m}$ is the plasma frequency and $k = \omega/c$ is the wave number in a vacuum.

We would like to know when the term in (9) containing $\nabla \cdot \mathbf{E}$ may be neglected. The time-harmonic $\mathbf{E}$ must drive $\mathbf{J}$ at the same frequency. Hence, (7) and (8) give us

$$\mathbf{J} = \frac{ie^2 n}{\omega m}\mathbf{E} = i\epsilon_0 \frac{\omega_p^2}{\omega}\mathbf{E}. \tag{10}$$

Then, taking the divergence of (4), we obtain

$$\nabla \cdot \mathbf{E} = -\frac{\mathbf{E} \cdot \nabla(\eta^2)}{\eta^2}, \tag{11}$$

where $\eta^2 = 1 - \frac{\omega_p^2}{\omega^2}$. In particular, as long as $\eta \neq 0$, this term vanishes when the inhomogeneity in $n(\mathbf{x})$ lies in a plane perpendicular to $\mathbf{E}$. Note also that when the variation in η is small compared to η itself, we may neglect this term regardless of the polarization of the electric field. However, for simplicity we will restrict ourselves to the two-dimensional problem with TE polarized waves, i.e., we will consider only functions $n(\mathbf{x}) = n(x, y)$ with $\mathbf{E}'(\mathbf{x}) = u(x, y)\mathbf{e_z}$, where $\mathbf{e_z}$ is the unit vector in the z-direction. This yields the equation of interest, the Helmholtz equation.

$$\Delta u(x, y) + k^2 \eta^2(x, y) u(x, y) = 0. \tag{12}$$

This equation also describes the scattering of TE-polarized waves by a dielectric medium. However, for plasmas the "index of refraction," η is always less than one instead of being larger than one as for normal dielectric materials. Furthermore, as soon as ω_p becomes larger than ω, η becomes purely imaginary and the wave attenuates quickly in the plasma. We denote by n_c the density at which $\omega_p = \omega$, also called the critical density.

α	$R^{(1)}(\%)$	$R^{(2)}(\%)$	$R^{(3)}(\%)$
0.10	0.06	0.07	0.07
0.25	0.43	0.51	0.52
0.50	2.53	2.90	2.94
0.75	9.98	11.00	11.11

Table 1: Reflection coefficients for various sharp interfaces and background densities

2.2 Ponderomotive Force

In seeking to understand how using the paraxial approximation affects the simulation of laser-plasma interactions, we must have some understanding of the mechanisms by which they interact. As discussed in the previous section, the varying plasma density influences the propagation of the laser. On the other hand, the laser influences the plasma primarily through the ponderomotive force.

We will not derive the ponderomotive force from the physics; see [9, p. 31–33] or [3, p. 305–309] for a more detailed discussion. Denoting the ponderomotive force by $\mathbf{F_p}$, we have

$$\mathbf{F_p} = -\frac{\epsilon_0}{4}\frac{\omega_p^2}{\omega^2}\nabla|\mathbf{E}|^2 \,. \tag{13}$$

Note that the ponderomotive force is proportional to the variation in the intensity. Hence in comparing the paraxial to the Helmholtz equation solutions we will compare not only the intensity, but also the magnitude of the intensity gradient.

2.3 Reflection from Sharp Interfaces

We now explore the reflection of a normal incidence wave by sharp interfaces to gain additional insight into the problem. Assume that an incident wave, $\mathbf{E_1} = e^{ik\eta_1 x}\mathbf{e_z}$, traveling in a region with $\eta = \eta_1$ encounters a sharp interface, $\eta = \eta_2$. (We have dropped the factor of $e^{-i\omega t}$ in the incident wave.) Solving Maxwell's equations with appropriate boundary conditions, one obtains [6, p. 33-1–33-11]

$$R = \frac{I_r}{I_i} = \frac{(\eta_1 - \eta_2)^2}{(\eta_1 + \eta_2)^2} \,, \tag{14}$$

where I_i and I_r are the intensities of the incident and reflected wave, respectively. The energy that is not reflected ends up in the transmitted wave. If the interface is not sharp, we will see less reflected light. Thus, we can get some idea of the maximum intensity we would see in the reflected wave from this ratio.

Table 1 lists the percentage of incident intensity in the reflected wave for various values of initial plasma density and three different sharp interfaces, (1) a ten-fold drop in plasma density, (2) a hundred-fold drop in plasma density and (3) a drop to a plasma density of zero. This last value gives an upper bound on the reflection with the given initial density. Hence, if the initial density is given by $n = \alpha n_c$, then

$$\begin{aligned}
\eta_1 &= \sqrt{1-\alpha} \,, \\
\eta_2^{(1)} &= \sqrt{1-\frac{\alpha}{10}} \,, \\
\eta_2^{(2)} &= \sqrt{1-\frac{\alpha}{100}} \,, \\
\eta_2^{(3)} &= 1 \,.
\end{aligned}$$

Notice that relatively little light reflects except in the case of high background density. One should bear in mind, however, that high-intensity lasers produce density *peaks* as well as density valleys. Therefore, even

α	$I^{(1)}_{max}$	$I^{(2)}_{max}$	$I^{(3)}_{max}$
0.10	1.05	1.05	1.05
0.25	1.14	1.15	1.15
0.50	1.34	1.37	1.37
0.75	1.73	1.77	1.78

Table 2: Maximum intensities in interfering incident and reflected waves

with a small background density at the beginning of the simulation, the plasma may develop significant density peaks and thereby observe significant reflection.

Furthermore, the effect of interference can also become quite important, even with small initial densities. For example, assume that the incident wave, $E_i = e^{ik\eta x}$, produces a reflected wave, $E_r = \beta e^{-ik\eta x + i\phi}$, where β is a positive real number and ϕ accounts for any phase shift in the wave. Then, the intensity of the *total* wave in front of the sharp interface is proportional to

$$\begin{aligned} I_{tot} &= |e^{ik\eta x} + \beta e^{-ik\eta x + i\phi}|^2 \\ &= 1 + \beta^2 + 2\beta\cos(2k\eta x + \phi)\,. \end{aligned}$$

This is a standing wave with twice the frequency of the incident wave with maximum value

$$\begin{aligned} I_{max} &= 1 + 2\beta + \beta^2 \\ &= (1+\beta)^2\,. \end{aligned}$$

If no interference takes place, we observe a total intensity proportional to $1 + \beta^2 < (1+\beta)^2 = I_{max}$. For normal incidence on a sharp interface, we have

$$\beta = \frac{|\eta_1 - \eta_2|}{|\eta_1 + \eta_2|}\,.$$

Table 2 lists the value of I_{max} for different background densities and sharp interfaces as in Table 1. As shown, this interference can substantially affect the intensity of the light in front of the interface. Also, the highly oscillatory intensity in front of the interface may increase the ponderomotive force and thereby influence the motion of the plasma. In particular, since the ponderomotive force is proportional to the gradient of the intensity, if one neglects interference, the ponderomotive force on the plasma in front of the interface would equal zero (for plane wave incident waves).

However, if we take the interference into account, the ponderomotive force is proportional to

$$\frac{d}{dx} I_{tot} = -4\beta k\eta_1 \sin(2k\eta_1 x + \phi)\,,$$

which may be quite large at certain values of x for high frequency waves.

3 Paraxial Approximation

We derive briefly the paraxial approximation and discuss its assumptions. Here we follow [5] quite closely. First, we write the Helmholtz equation in the following form

$$(P^2 + Q^2)u = 0\,, \tag{15}$$

where

$$\begin{aligned} P &= \frac{\partial}{\partial x}\,, \\ Q &= (\Delta_\perp + k^2\eta^2)^{1/2}\,, \\ \Delta_\perp &= \frac{\partial^2}{\partial y^2} + \frac{\partial^2}{\partial z^2}\,. \end{aligned}$$

(This holds for three dimensions. In two dimensions, $\Delta_\perp = \frac{\partial^2}{\partial y^2}$.) Equation (15) is equivalent to

$$\{(P+iQ)(P-iQ)+i[P,Q]\}\,u = 0\,, \tag{16}$$

where $[P,Q] = PQ - QP$. The paraxial approximation first assumes that $[P,Q] \approx 0$. Roughly speaking, this assumption holds when η varies little in the x-direction. Considering only forward traveling wave solutions, this leaves

$$\frac{\partial u}{\partial x} = iQu\,. \tag{17}$$

This approximation explicitly removes any backscattered waves. As pointed out in Section 2.3, we do indeed expect very little backscatter when the refractive index varies slowly.

One can easily verify that

$$Q = (Q+k\eta)^{-1}\Delta_\perp + k\eta + k(Q+k\eta)^{-1}[\eta, Q]\,. \tag{18}$$

We now assume that $[n,Q] \approx 0$. This condition holds when η varies slowly in the y- and z-directions. In particular, this implies that we expect to see very little scattering in any direction transverse to the incident wave. In addition, under these conditions, we assume that $\eta \approx \eta_0$ in the first term of (18), where η_0 is a function of x only. One may think of η_0 as an average or background refractive index. After some manipulation, this leaves

$$Q \approx (\Delta_\perp + k^2\eta_0^2)^{1/2} + k(\eta - \eta_0)\,. \tag{19}$$

We use this form of the paraxial approximation.

Remark. There are other perhaps more widely used forms of the paraxial approximation. In particular, by assuming that $\Delta_\perp \ll k^2\eta_0^2$ we can linearize the square root in (19) to obtain

$$Q \approx \frac{1}{2k\eta_0}\Delta_\perp + k\eta\,.$$

However, we choose not to make this additional approximation.

4 Numerical Methods

To compare the paraxial approximation to the full solution of the Helmholtz equation, we need an implementation of each approach. For the paraxial approximation, we use a code written by Dorr and Garaizar [4] following the approach in [1]. The full Helmholtz solver is based on the method introduced by Bruno and Sei [2]. In the following sections we describe these implementations briefly.

4.1 Paraxial Approximation Implementation

Because we expect the solution to have only a small transverse component, we make the following change of unknown

$$u(x,y) = U(x,y)e^{ik\int_{x_0}^{x}\eta_0(x')\,dx'}\,, \tag{20}$$

where η_0^2 is the average of η^2 in y. More clearly, since $\eta^2 = 1 - \frac{\omega_p^2}{\omega^2}$ and since ω_p^2 depends linearly on the electron density, η_0^2 corresponds to the average of the electron density in y. From (19) and (17) we then obtain

$$\frac{\partial U}{\partial x} = i\left[(\Delta_\perp + k^2\eta_0^2)^{1/2} - k\eta_0\right]U + ik(\eta - \eta_0)U\,. \tag{21}$$

We then approximate $\eta - \eta_0$ by assuming that this difference is small. Let ω_{p0}^2 be the average of ω_p^2 in y. Then, considering η to be a function of ω_{p0}^2, we expand $\eta - \eta_0$ about ω_{p0}^2 using a first-order Taylor

approximation

$$\begin{aligned}\eta - \eta_0 &= \sqrt{1-\frac{\omega_p^2}{\omega^2}} - \sqrt{1-\frac{\omega_{p0}^2}{\omega^2}} \\ &\approx -\frac{\frac{\omega_p^2}{\omega^2} - \frac{\omega_{p0}^2}{\omega^2}}{2\sqrt{1-\frac{\omega_{p0}^2}{\omega^2}}} \\ &= \frac{\eta_0}{2}\left(\frac{\eta^2}{\eta_0^2} - 1\right) .\end{aligned}$$

Hence, we arrive at

$$\begin{aligned}\frac{\partial U}{\partial x} &= i\left[(\Delta_\perp + k^2\eta_0^2)^{1/2} - k\eta_0\right]U + i\frac{k\eta_0}{2}\left(\frac{\eta^2}{\eta_0^2} - 1\right)U \qquad (22)\\ &= (D+R)\,U\,, \qquad (23)\end{aligned}$$

where

$$\begin{aligned}D &= i\left[(\Delta_\perp + k^2\eta_0^2)^{1/2} - k\eta_0\right] \\ R &= i\frac{k\eta_0}{2}\left(\frac{\eta^2}{\eta_0^2} - 1\right) .\end{aligned}$$

One may think of the operators D and R as a diffraction and refraction operators, respectively. They separate the differentiation with respect to y from the variation of η in y.

To generate a solution for (23), we use operator splitting

$$\begin{aligned}\frac{\partial U}{\partial x} &= RU \qquad (24)\\ \frac{\partial U}{\partial x} &= DU\,. \qquad (25)\end{aligned}$$

We then take alternating steps in x, using the output of the last for the input of the next thereby propagating the solution forward. Formally, we write

$$U(x+\Delta x, y) = U(x,y)e^{\frac{\Delta x}{2}R}e^{\Delta x D}e^{\frac{\Delta x}{2}R}\,. \qquad (26)$$

Hence, more specifically, we take a half-step with R, a full-step with D and then another half-step with R. This method has an error proportional to $(\Delta x)^3$ [5, p. 635].

Solving (24) amounts to a simple integration in x. Using the midpoint rule, we obtain

$$U(x+\Delta x/2, y) = U(x,y)\exp\left\{i\frac{k\eta_0(x+\Delta x/4)}{2}\left[\frac{\eta^2(x+\Delta x/4, y)}{\eta_0^2(x+\Delta x/4)} - 1\right]\right\} . \qquad (27)$$

To solve equation (25), we impose periodic boundary conditions on the domain in the y-direction and compute the Fourier components of the solution. This removes any difficulties associated with the square root in the operator since the operator is diagonal in Fourier space. Note that although periodic boundary conditions are not technically correct, as long as the domain has a large enough extent in the y-direction, the laser intensity will be so small that imposing a periodic condition does not introduce too much error. Let

$$U(x,y) = \sum_{j=-\infty}^{\infty} U_j(x)e^{ik_j y}\,, \qquad (28)$$

where $k_j = \frac{2\pi}{L}j$ and L is the size of the domain in the y-direction.

By direct calculation we see that applying D to U multiplies the Fourier components $U_j(x)$ by $(-k_j^2 + k^2\eta_0^2)^{1/2} - k\eta_0$. Hence solving (25) in Fourier space using the midpoint rule yields

$$U_j(x+\Delta x) = U_j(x)\exp\left(i\Delta x\left\{\left[-k_j^2 + k^2\eta_0^2(x+\Delta x/2)\right]^{1/2} - k\eta_0(x+\Delta x/2)\right\}\right) . \qquad (29)$$

Of course, we then use (28) to compute $U(x+\Delta x, y)$. By using the fast Fourier transform we can thereby compute these solutions very efficiently.

Given an initial wave profile, we use (27) and (29) and follow the formal description of the algorithm given by (26) to propagate the solution. This method allows us to efficiently compute solutions to the paraxial wave equation over large domains.

4.2 Helmholtz Equation Solver

We now give a brief description of the implementation of the full Helmholtz equation solver. Assume that there exists a compact subset of the plane, Ω, such that

$$\eta(x,y) = \eta_0\,,\ (x,y) \notin \Omega\,.$$

Then, we find the solution of the Helmholtz equation by inverting the Lippmann-Schwinger integral equation

$$u(\mathbf{x}) = u^i(\mathbf{x}) - \frac{i(k\eta_0)^2}{4}\int_\Omega H_0^1(k\eta_0|\mathbf{x}-\mathbf{y}|)m(\mathbf{y})u(\mathbf{y})\,d\mathbf{y}\,, \tag{30}$$

where $\mathbf{x}$ and $\mathbf{y}$ are two-component vectors, $u^i(\mathbf{x})$ is the incident wave and

$$m(\mathbf{x}) = 1 - \frac{\eta^2(\mathbf{x})}{\eta_0^2}\,.$$

The incident wave must satisfy

$$\Delta u^i + k^2\eta_0^2 u^i = 0$$

in the entire plane. Notice that $m(\mathbf{x}) = 0$ for $\mathbf{x} \notin \Omega$. An accurate and efficient solution to this integral equation relies on accurate and efficient methods (1) to compute the integral in (30) and (2) to solve the associated linear system.

Since Ω is compact we can find a disc centered at the origin with radius R such that $\Omega \subset R$. We can then perform the integral in polar coordinates. However we first make use of the following important addition theorem (see [2])

$$H_0^1(k\eta_0|ae^{i\phi} - re^{i\theta}|) = \sum_{l=-\infty}^{\infty} \mathcal{J}_l(a,r)e^{il(\phi-\theta)}\,, \tag{31}$$

where

$$\mathcal{J}_l(a,r) = J_l(k\eta_0\,\min(a,r))H_l^1(k\eta_0\,\max(a,r))$$

and where we associate $\mathbf{x}$ with $ae^{i\phi}$ and $\mathbf{y}$ with $re^{i\theta}$. If we also express $u(\mathbf{x})$ and $u^i(\mathbf{x})$ in polar coordinates as Fourier series in their angular variable for each radius,

$$u(a,\phi) = \sum_{l=-\infty}^{\infty} u_l(a)e^{il\phi}$$

$$u^i(a,\phi) = \sum_{l=-\infty}^{\infty} u_l^i(a)e^{il\phi}\,,$$

then after some manipulation we obtain

$$u_l(a) = u_l^i(a) - \frac{i(k\eta_0)^2}{4}\int_0^R \mathcal{J}_l(a,r)\int_0^{2\pi} m(r,\theta)u(r,\theta)e^{-il\theta}\,d\theta\,r\,dr\,. \tag{32}$$

We then truncate the Fourier series and solve this system of equations for $l = -M \ldots M$ for some positive integer M. As we increase M the truncated series converges to the true solution at a rate that depends on the smoothness of the solution.

We restrict our attention to cases in which the electron density and hence also η and m are smooth functions in the plane. In this case u is also smooth and the Fourier series converges rapidly. In this case,

the trapezoidal rule also evaluates the angular integral in (32) to high-order accuracy. (In fact, the trapezoidal rule gives exponential accuracy when integrating over the period of an analytic periodic function.) The fast Fourier transform provides efficient evaluation of this integral.

For the radial integration define

$$I_l(r) = \int_0^{2\pi} m(r,\theta)u(r,\theta)e^{-il\theta}\,d\theta\,.$$

For each radial discretization point, $0 \le a \le R$, we must evaluate

$$H_l^1(k\eta_0 a)\int_0^a J_l(k\eta_0 r)I_l(r)\,dr \tag{33}$$

and

$$J_l(k\eta_0 a)\int_a^R H_l^1(k\eta_0 r)I_l(r)\,dr\,. \tag{34}$$

Without discussing too many complicating details, we accomplish this by approximating $I_l(r)$ with a truncated Chebyshev series,

$$I_l(r) \approx \sum_{k=0}^{N} c_k^{(l)} T_k(r)\,,$$

on each of several subintervals of $[0, R]$. We complete the integration by evaluating moments of the form

$$\int_0^a J_l(k\eta_0 r)T_k(r)\,dr$$

and

$$\int_a^R H_l^1(k\eta_0 r)T_k(r)\,dr\,.$$

The associated linear system is non-symmetric and indefinite. Hence we use the Generalized Minimal Residual (GMRES) iterative method for solving linear systems. GMRES requires only a matrix vector product and performs well for several examples including those shown in this paper. However, as the problem size increases ($k\eta_0 R \gg 1$) and as the contrast between the inhomogeneity and the background refractive index grows, GMRES convergence typically slows and computation of solutions becomes infeasible. Well-chosen preconditioners can partially remedy this problem, but the problem of computing the scattering from electrically large bodies remains a difficult and active field of research.

5 Examples

Using the implementations described above we directly compare the paraxial and the Helmholtz equation solutions. Denote the Helmholtz equation solution by $u^{(h)}$ and the paraxial equation solution by $u^{(p)}$. In the following we compare the solutions for three different electron density functions. We discuss the scattering from a single density valley (a region of decreased electron density), from multiple peaks (regions of increased electron density) and valleys and, finally, from a density function given by actual output from a laser-plasma interaction simulation.

We compute each solution on a grid that is fine enough to ensure sufficient convergence and then compute the solution intensities, $I^{(h)} = |u^{(h)}|^2$ and $I^{(p)} = |u^{(p)}|^2$. After interpolating the Helmholtz solution intensity from its polar grid to the paraxial solution's Cartesian grid we compute the pointwise difference in intensity. Since the maximum intensity varies significantly with the background electron density for a given arrangement of inhomogeneities, we then divide by the maximum of the Helmholtz solution intensity to obtain a type of relative error. More precisely, given a common grid $\mathcal{G}$, we compute

$$e_r(x,y) = \frac{I^{(h)}(x,y) - I^{(p)}(x,y)}{I_{\max}^{(h)}}\,, \quad (x,y) \in \mathcal{G}\,, \tag{35}$$

n_0/n_c	$e_r^{\max}(\%)$
0.10	2.62
0.25	7.16
0.50	50.2
0.75	89.8

(a) Single Valley

n_0/n_c	$e_r^{\max}(\%)$
0.10	5.04
0.25	10.9
0.40	25.0
0.60	63.9

(b) Multiple Peaks and Valleys

Table 3: Comparison of $e_r^{\max}$ for various background densities

where

$$I_{\max}^{(h)} = \max_{(x,y)\in\mathcal{G}} I^{(h)}(x,y)\,.$$

This relative error allows us to compare the methods over a range of background densities.

5.1 A Single Valley

In typical laser-plasma simulations several separate density peaks and valleys develop due to the plasma motion and the ponderomotive force (see Figure 2(a)). These peaks and valleys are long in the direction of laser propagation, but narrow in the transverse direction. Hence, we first examine the scattering from a single long and narrow density valley in a variety of background densities.

Of course, since single valleys do not arise in actual simulations we propose an approximate analytical description of the valley. The valleys may dip as low as $10^{-2}n_0$ where n_0 is the background density. (This value is not critical, however, because as shown in Tables 1 and 2, we would not expect the scattering to depend strongly on the valley depth.) Hence we use the following density function

$$n(x,y) = \begin{cases} n_0\left[1 - \frac{99}{100}\cos^2\left(\frac{\pi}{2}\left[\frac{x^2}{8^2} + \frac{y^2}{1^2}\right]\right)\right], & \text{if } \frac{x^2}{8^2} + \frac{y^2}{1^2} < 1 \\ n_0\,, & \text{otherwise.} \end{cases} \tag{36}$$

This valley has a minimum of $10^{-2}n_0$ and its support coincides with the set of points (x,y) such that $x^2/8^2 + y^2/1^2 \le 1$, where the unit of measure is one vacuum wavelength of the incident light. The boundary of this set is an ellipse with major axis of 8 and minor axis of 1. The incident plane wave has unit intensity and propagates parallel to the x-axis. The plots of solution intensities and relative error for a background electron density $n_0 = 0.5n_c$ are found in Figure 1(a–c). In these plots, the x-axis lies along the line of the sharp intensity peaks.

Table 3(a) shows the maximum absolute value of the relative error,

$$e_r^{\max} = \max_{(x,y)\in\mathcal{G}} e_r(x,y)\,,$$

for several other background densities. Notice the strong agreement for $0.1n_c$. At the same time, one observes strong disagreement for $0.75n_c$. On the other hand, we should mention that for density values this large, the original model may even be called into question.

Density valleys such as the one we are considering focus the light into a series of intensity peaks. These peaks contribute significantly to the ponderomotive force. The plots in Figure 1(a–c) show that the paraxial solution disagrees with the Helmholtz solution in both the height and location of the sharp peaks. One could speculate that this difference might be caused by either the paraxial solution's lack of backscatter and the associated interference or its damping of high-order transverse modes, which could alter the location of sharp foci.

5.2 Multiple Peaks and Valleys

Now we consider multiple peaks and valleys each in the form (36). We attempt to construct a simple small model of a laser-plasma simulation density profile as typified by Figure 2(a). One often observes two long

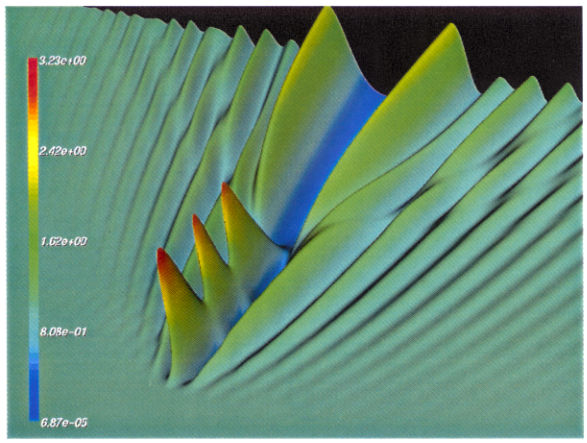

(a) Paraxial Solution Intensity ($I^{(p)}$)

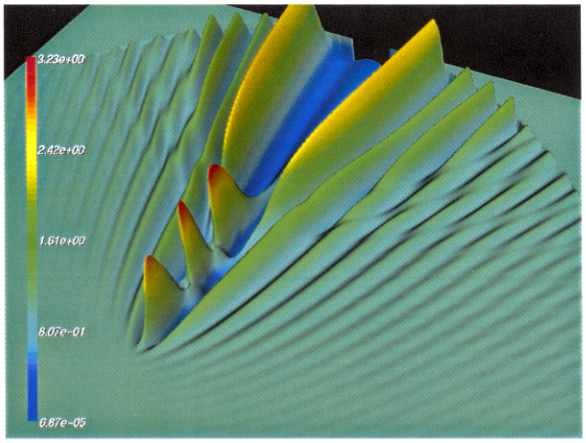

(b) Helmholtz Solution Intensity ($I^{(h)}$)

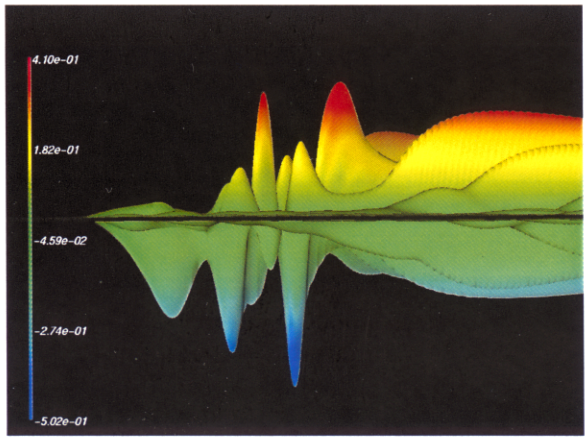

(c) Relative Error (e_r)

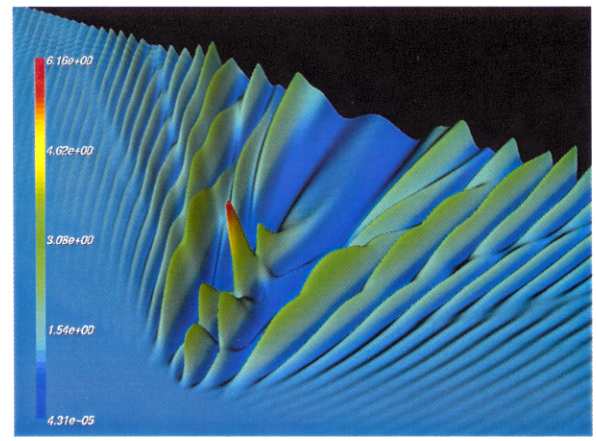

(d) Paraxial Solution Intensity ($I^{(p)}$)

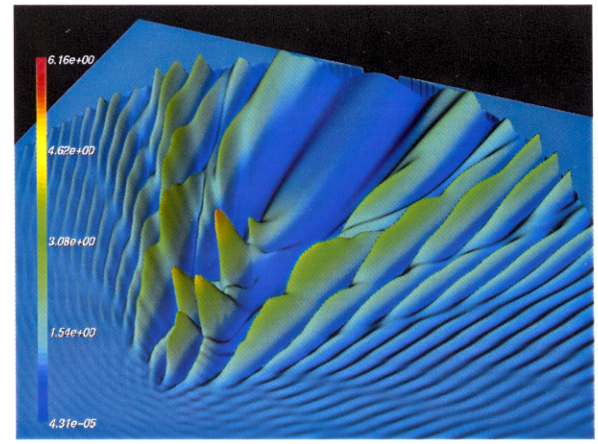

(e) Helmholtz Solution Intensity ($I^{(h)}$)

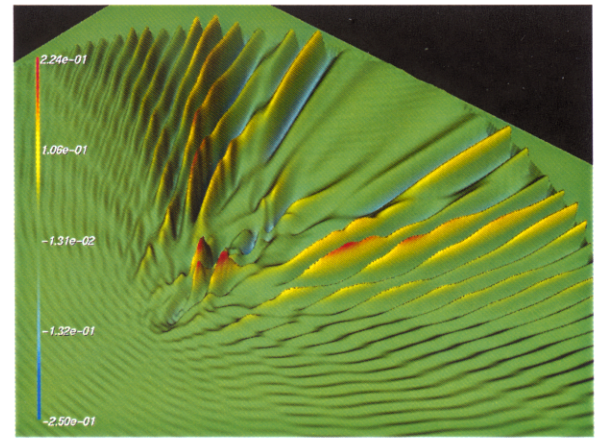

(f) Relative Error (e_r)

Figure 1: Intensities and error for a single valley (a–c) and multiple peaks and valleys (d–f)

density peaks on either side of several smaller peaks and valleys. We have observed that the density peaks may rise as high as $1.5n_0$–$1.75n_0$. In this example all peaks rise to $1.5n_0$ and all valleys dip to $10^{-2}n_0$.

We place two elliptical peaks with major and minor axes of 8 and 2, respectively, parallel to the x-axis and with centers separated by 6 vacuum wavelengths. Then, between these peaks, running parallel to the x-axis with centers separated by 5 vacuum wavelengths, we place a valley, a peak and another valley. The two valleys have major and minor axes of 3 and 1, respectively, and the peak has major and minor axes of 2 and 1, respectively.

The plots of solution intensities and relative error for a background density of $0.4n_c$ appear in Figure 1(d–f). As in the previous example, the valleys focus the light into several intensity spikes. At the same time, the density peaks bend the light away from their centers, further channelling and concentrating the light in the center. One observes that the peaks in the paraxial and the Helmholtz solution differ significantly in height. Furthermore, the intensity of the light propagating out at an angle from the primary peaks seems to be larger in the Helmholtz solution than in the paraxial solution.

Table 3(b) lists the maximum absolute value of the relative error for various background densities. As for the single valley, one quickly observes that the agreement between paraxial and Helmholtz intensities increases as background density decreases.

5.3 Densities From Simulation Data

The careful examination of these simple examples provides insight and intuition for the more general problem. At the same time, a density profile generated by an actual laser-plasma simulation provides perhaps a more relevant comparison. After all, if we observe no significant difference in such an example then one could dismiss the differences observed in the simple examples as contrived or coincidental.

In this example, the code developed by Dorr and Garaizar [4], which uses the paraxial approximation discussed in this paper for the light propagation, provides the density profile as shown in Figure 2(a). This was produced by a simulation of a CH-plasma, initially at rest, with an initial background density of $0.5n_c$ and an average ionization number of 3.5. A 1 micron wavelength laser with 2×10^{15} W/cm^2 peak intensity and a width of 40 wavelengths illuminated the plasma in a 64×64 wavelength domain for approximately 50 picoseconds.

To avoid any anomalous edge reflections, we need to smooth the density profile to the background density. Outside a disc with a 60 wavelength diameter centered in the domain we set the density to the background density $0.5n_c$. Then, over 4 wavelengths at the edge of the disc, we smooth the density profile from its computed value to the background density.

Figure 2 provides plots of the density profile, the paraxial and Helmholtz intensities and the relative error. Once again we note significant difference in the height of the peaks. Furthermore, it appears that the methods agree rather well on the first peak, but that the remaining peaks oscillate in height exactly opposite of each other. More specifically, when the Helmholtz intensity has a large peak, the corresponding peak in the paraxial intensity is smaller and vice versa.

6 Conclusion

The paraxial approximation makes the simulation of large-scale laser-plasma interactions possible. The full Helmholtz equation (or Maxwell equations) remains too difficult to solve for such large computational domains. However, as shown in this paper, the paraxial approximation may fail to produce sufficiently accurate results especially in high-density plasmas. Certainly, as shown, typical examples for which the background density approaches or exceeds $0.4n_c$ may produce significant errors. At the same time, because of the many adjustable parameters, i.e., simulation time, domain size, laser intensity and profile, and the extremely complicated phenomena associated with laser-plasma interactions, there are not simple, absolute criteria for determining when a solution is accurate and when it is not.

Future research directions include an analysis of the source of the discrepancies that we have observed. We might then be able to remedy some of the error introduced by the approximations. One might also develop *a posteriori* error estimates. These would allow one to determine when the paraxial approximation holds, although they would still not allow simulation at higher denstities.

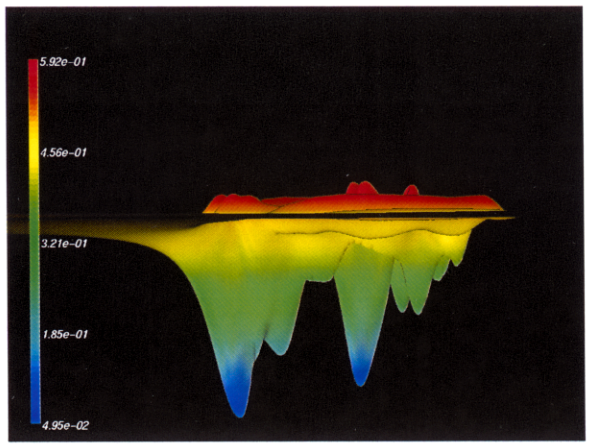

(a) Electron Density (n/n_c)

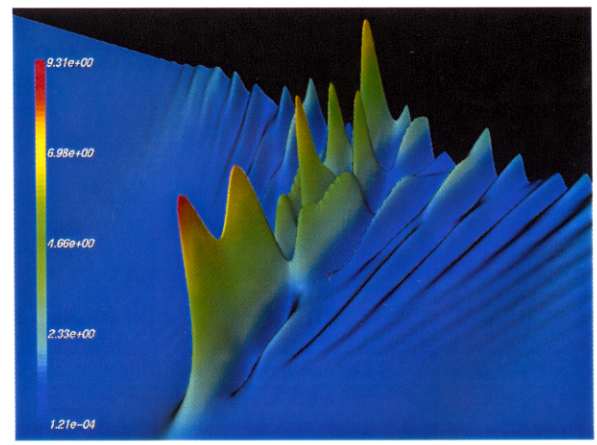

(b) Paraxial Solution Intensity ($I^{(p)}$)

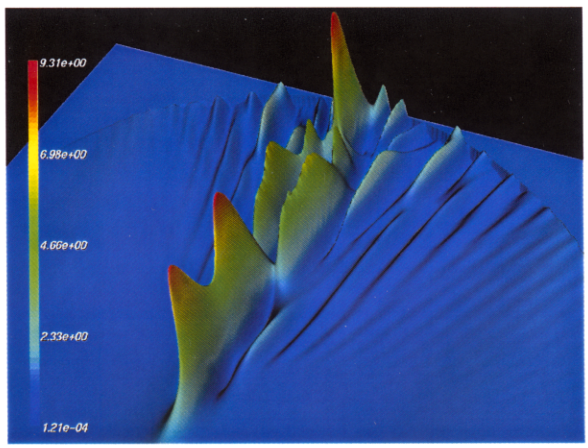

(c) Helmholtz Solution Intensity ($I^{(h)}$)

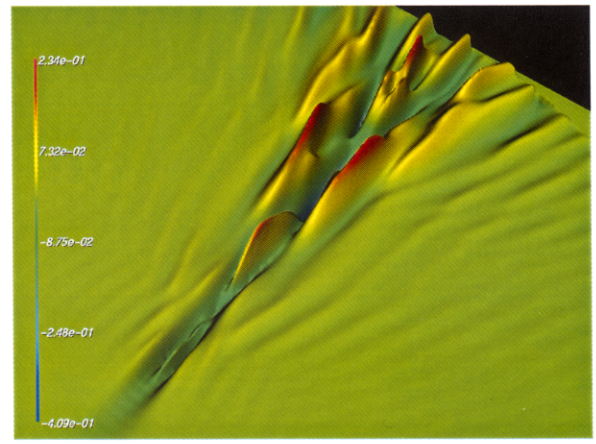

(d) Relative Error (e_r)

Figure 2: Electron density from laser-plasma simulation, intensities and error

7 Acknowledgments

The author gratefully acknowledges support under a U.S. Department of Energy Computational Science Graduate Fellowship. The plots in this paper were produced using the Vizamrai tool developed by Steven Smith at Lawrence Livermore National Laboratory.

References

[1] R. L. Berger, B. F. Lasinski, T. B. Kaiser, E. A. Williams, A. B. Langdon, and B. I. Cohen. Theory and three-dimensional simulation of light filamentation in laser-produced plasma. *Phys. Fluids B*, 5(7):2243–2258, July 1993.

[2] Oscar P. Bruno and Alain Sei. A fast high-order solver for problems of scattering by heterogeneous bodies. to appear, IEEE Transactions in Antenna Propagation.

[3] Francis F. Chen. *Introduction to Plasma Physics and Controlled Fusion*, volume 1. Plenum Press, NY, 2nd edition, 1984.

[4] Milo R. Dorr and F. Xabier Garaizar. Simulation of laser filamentation using adaptive mesh refinement. in preparation.

[5] M. D. Feit and J. A. Fleck, Jr. Beam nonparaxiality, filament formation, and beam breakup in the self-focusing of optical beams. *Journal of the Optical Society of America B*, 5(3), 1988.

[6] Richard P. Feynman, Robert B. Leighton, and Matthew Sands. *The Feynman Lectures on Physics*, volume 2. Addison-Wesley, MA, 1964.

[7] Göran Frenning. *Radio wave propagation and linear resonance absorption in an inhomogeneous, cold, unmagnetised plasma.* PhD thesis, Swedish Institute of Space Physics, Uppsala University, Uppsala Sweden, April 1999.

[8] C. S. Liu and V. K. Tripathi. *Interaction of Electromagnetic Waves with Electron Beams and Plasmas.* World Scientific, NJ, 1994.

[9] Dwight R. Nicholson. *Introduction to Plasma Theory.* Krieger, FL, 1983.